SPATIAL AND TEMPORAL IONOSPHERIC MONITORING USING BROADBAND SFERIC MEASUREMENTS

A Thesis
Presented to
The Academic Faculty

by

Jackson C. McCormick

In Partial Fulfillment
of the Requirements for the Degree
Master's of Science in the
School of Electrical and Computer Engineering

Georgia Institute of Technology
December 2015

SPATIAL AND TEMPORAL IONOSPHERIC MONITORING USING BROADBAND SFERIC MEASUREMENTS

Approved by:

Professor Morris Cohen, Advisor
School of Electrical and Computer Engineering
Georgia Institute of Technology

Professor Paul Steffes
School of Electrical and Computer Engineering
Georgia Institute of Technology

Professor Malcolm Bibby
School of Electrical and Computer Engineering
Georgia Institute of Technology

Professor Sven Simon
School of Earth and Atmospheric Science
Georgia Institute of Technology

Date Approved: December 3rd, 2015

To my wife,

Holly McCormick

ACKNOWLEDGEMENTS

First and most importantly, I would like to thank my wife and the love of my life, Holly McCormick, who has always been there for me. Without her, our transition to Atlanta and graduate school would not be a fraction of what it has been. She is without a doubt the most important part of my life.

My family has shaped who I am. Thanks to thank my Dad for instilling in me a desire and passion to learn and to study the world. My Mom has always been there for me through all the years, always rooting for me. My brother William, who pushed me to get better in my years of athletic competition, a lesson well learned. And to my sister Carly for all the great memories and friendship.

A hearty thanks goes out to Morris Cohen, who has been a fantastic advisor and mentor, more so than I ever hoped for. I look forward to working with you for a few more. My introduction to LF/VLF research has been a great ride, and working with him and the lab he has created has been amazing.

I would like to thank my new lab-mates and friends for all of the fun and memories. My experience at Georgia Tech would not be the same without them. I would like to especially thank Nicholas Gross for the many helpful talks and suggestions. He has been invaluable to my early years in graduate school and this work.

Many thanks to my committee members, Dr. Paul Steffes, Dr. Malcolm Bibby, and Dr. Sven Simon for taking the time to review my thesis and provide many helpful comments.

TABLE OF CONTENTS

LIST OF TABLES

LIST OF FIGURES

SUMMARY

The objective of this thesis is to use radio emissions from lightning, known as 'radio atmospherics' or 'sferics', to study the temporal and spatial variation of the lower ionosphere, a layer of ionized atmosphere beginning at ∼70 km altitude (D-region). Very Low Frequency (VLF, 3−30kHz) radio waves are a useful diagnostic for lower ionospheric monitoring due to their reflection from this region and global propagation. Traditionally, the lower ionosphere has been sensed using single-frequency VLF transmitters allowing for analysis of a single propagation path, as there are only a small number of transmitters.

A lightning stroke, however, releases an intense amount of impulsive broadband VLF radio energy in the form of a sferic, which propagates through the Earth-ionosphere waveguide. Lightning is globally distributed and very frequent, so a sferic is therefore also a useful diagnostic of the D-region. This is true both for ambient or quiet conditions, and for ionospheric perturbations such as solar flare x-ray bursts. Lightning strokes effectively act as separate VLF transmitting sources. As such, they uniquely provide the ability to add a spatial component to ionospheric remote sensing, in addition to their broadband signature which cannot be achieved with man-made transmitters.

We describe the methods of processing in detail. As an example, we analyze a solar flare during which time there is a significant change in magnitude and frequency content of sferics. This disturbance varies with distance from the source, as well as time. We describe the methods of processing in detail, and show results at Palmer Station, Antarctica for both a quiet and active solar day.

CHAPTER I

INTRODUCTION

1.1 Background

Lightning strokes generate powerful impulsive broadband radio waves in the Very Low Frequency (VLF, 3−30 kHz) and Low Frequency (LF, 30−300 kHz) frequency bands known as 'radio atmospherics' or 'sferics'. Sferics propagate to global distances guided by Earth-ionosphere waveguide system, made up of the Earth ground and the 'D-region' of the ionosphere (∼70−85 km). Sferics are very sensitive to the current conditions of the ionosphere and even small perturbations will modify the reflection from the D-region, and in turn the measured waveform at a distance.

While the E and F-regions of the ionosphere (100−500 km) have been heavily measured and are reasonably accurately estimated by the empirically-constructed International Reference Ionosphere [*Bilitza and Reinisch*, 2008], the D-region is much harder to characterize as it is too high for balloons and too low for satellites. The IRI largely fails at estimating D-region parameters.

The D-region varies due to solar diurnal effects and on a seasonal basis. It also varies on a spatial and time scale due to transient perturbations such as solar flares as discussed in *Mitra* [1964], Lightning-induced Electron Precipitation (LEP) described in *Helliwell et al.* [1973], or electromagnetic pulses from lightning [*Inan et al.*, 1991].

Rocket based measurements may produce good ionospheric profile results [*Sechrist*, 1974; *Kintner et al.*, 1983; *Friedrich and Torkar*, 2001], but they cannot realistically be applied on a continuous and global basis. These rocket based measurements have shown a highly variable ionosphere on a time, location, and seasonal scale. The most important parameter in determining current D-region ionospheric conditions is the

electron density profile with altitude. Although it is not in general known precisely, the D-region electron density profile is often assumed to be an exponential increase with altitude, which can be characterized with an effective height and a sharpness described by Equation 1

$$N_e(H) = 1.43 \,\mathrm{x}\, 10^7 \exp(-0.15H') \cdot \exp[(\beta - 0.15)(H - H')] \quad \mathrm{cm}^{-3} \tag{1}$$

where H', is in km, and β is in km^{-1}. These are known as the Wait parameters [*Wait and Spies*, 1964]. H' is the effective 'height', and β is the 'sharpness' of the D-region of the ionosphere. Looking at several rocket-based measurements, the exponential trend is visible especially in Figure 1 at the heights of 60-90 km near the D-region.

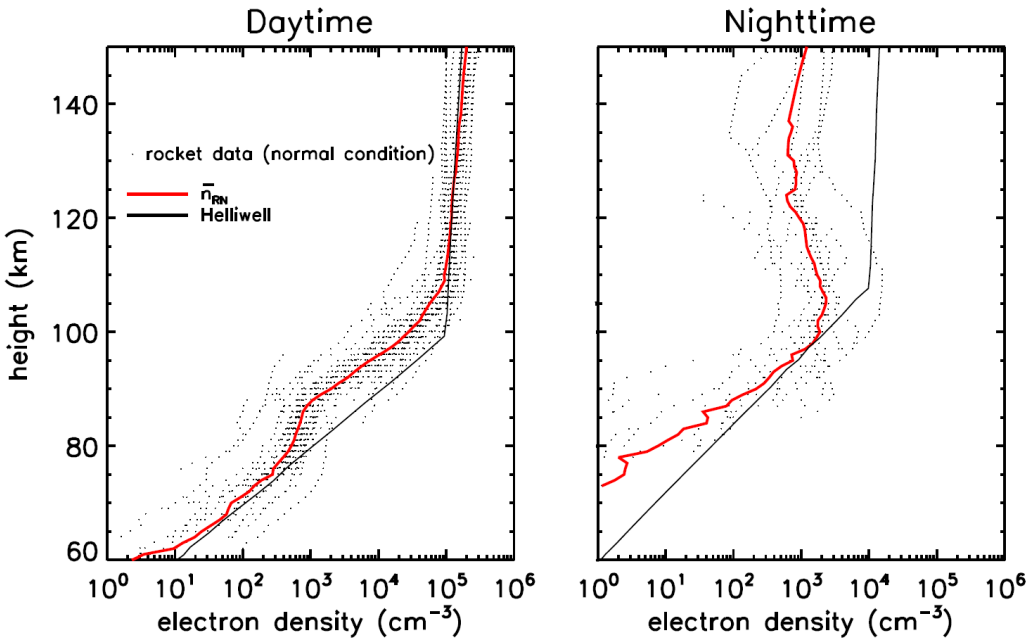

Figure 1: Plot of rocket measured electron density height profiles. Plot taken from [*Tao et al.*, 2010].

Of secondary importance in determining ionospheric conditions is the collision frequency, which is closely connected with the neutral atmospheric density.

Lightning flashes occur about 40−50 times per second throughout the Earth. The

global occurrence of lightning, along with the sensitivity to the current ionospheric conditions, makes sferics a convenient and ever-present probe of the D region of the ionosphere. Using this hypothesis, *Cummer et al.* [1998]; *Cheng et al.* [2006]. developed a technique to monitor the ionospheric electron density parameters H', β using sferics with known lightning locations. This method was expanded upon using a Finite-Difference Time-Domain (FDTD) simulation, to interpret the received waveforms to infer Mid-latitude diurnal variations of day and nighttime, and the D-region sharpness β [*Han and Cummer*, 2010a, b; *Han et al.*, 2011].

Because of the low attenuation in the Earth-ionosphere waveguide, and VLF waves are able to penetrate significantly into water via the skin effect, various navies have constructed and operated VLF transmitters for the purposes of submarine communications. These transmitters operate almost continuously at constant power and frequency allowing an observer to serendipitously use them to monitor the current conditions of the ionosphere. *Thomson* [1993]; *McRae and Thomson* [2000]; *Thomson et al.* [2007]; *Thomson and McRae* [2009]; *Thomson* [2010] have used these VLF transmitters along with H' and β and the Long Wave Propagation Capability (LWPC) model, to measure and monitor H' and β. The LWPC was developed to model VLF transmitter propagation throughout the Earth-ionosphere waveguide and has seen many improvements and updates. The latest version is described in [*Ferguson*, 1998].

The nighttime D-region is ionized primarily by galactic cosmic rays, x-rays (<1nm), and Lyman-α (121.6 nm) radiation emission from hydrogen. During day time it is dominantly ionized by Lyman-α radiation *Kockarts* [2002]. However, during a x-ray solar flare, the D-region ionization is dominated by the photoionization of the atmospheric gases [*Grubor et al.*, 2008]. Using an FDTD model to interpret received VLF sferics, *Han and Cummer* [2010a] inferred H', β during summer months including during solar flares. Many have used VLF transmitters and LWPC to infer the Wait parameters during solar flares [*Thomson and Clilverd*, 2001; *McRae and Thomson*,

2004; *Thomson et al.*, 2005; *Grubor et al.*, 2008; *Dahlgren et al.*, 2011; *Singh et al.*, 2013; *Kolarski and Grubor*, 2014; *Šulić and Srećković*, 2014].

1.2 Organization

The objective of this research is to develop a technique to use broadband sferics to monitor the ionosphere spatially and temporally. This will allow for sensing of disturbances on the ionosphere such as solar flares. The remainder of this thesis is organized as follows:

Chapter 2 describes the different data sources used in the analysis and some of the difficulties and measurement errors these systems have.

Chapter 3 introduces the complications of using broadband data and the steps needed to increase the quality of the representative sferics and mitigate unavoidable errors in the timing.

Chapter 4 displays the capabilities of this research and analysis. It also provides an analysis of the measured results. Lastly, it concludes the work with a final summary and offers final remarks.

CHAPTER II

DATA DESCRIPTION

2.1 Time-Series Broadband Data

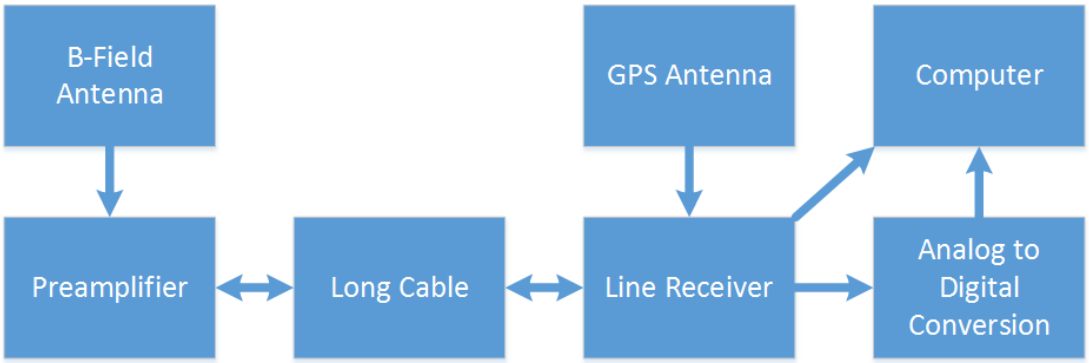

Figure 2: Block diagram of the VLF instrument at Palmer Station, Antarctica described in this section.

We utilize the magnetic field emitted from lightning strokes recorded at a distance using radio receivers on the ground. The time-series data used in this work was sampled by an a VLF instrument at Palmer Station, Antarctica (Lat/Lon: -64.775/-64.051). This instrument is similar in nature to the AWESOME instrument described in *Cohen et al.* [2010]. The instrument at Palmer utilizes two orthogonal wire-loop antennas orthogonal to each other and the ground. These loop antennas are sensitive to the magnetic field of incident fields and can detect signals in the fT/rt-Hz range.

In the frequency band of interest, the primary sources of interference are power lines and switching noise. Power lines operate at 50 or 60 Hz, but depending on the power quality, harmonics can be generated into the kHz range. The antenna is therefore mounted as far away from potential interference sources as possible, and connected immediately to a preamplifier. The preamplifier matches to the antenna

and then the data is amplified with a low noise amplifier. A long communications cable connects the preamplifier to a line receiver. This cable helps to isolate the antenna from interference, such as AC power which powers the line receiver.

The magnetic field is sampled at 100 kHz, which results in a Nyquist frequency of 50 kHz. The first channel samples data on the rising edge of the clock, while the second samples on the falling edge. This is easily corrected in post-processing. Since the loop antenna is sensitive to frequencies higher than the sampled data, an anti-aliasing filter is employed to ensure minimal aliasing distortion. The data is therefore filtered in the front-end of the line receiver.

The system utilizes GPS timing information in order to generate an absolute timing reference (100 ns or better) and generate a time-synced clock. This allows data recorded at multiple sites around the world to have the same absolute reference and be directly comparable. The data is then sampled using a National Instruments data acquisition card with 16 bits of resolution resulting in 96 dB of dynamic range and stored on a local computer.

The receiver is calibrated, and its frequency response is shown below in Figure 3 and the noise response is shown in Figure 4. There are a few differences between the receiver at Palmer Station and that of the AWESOME receiver. The impedance of the Palmer Station antenna is 4 mΩ and 65 μH, compared to the 1 Ω, 1 mH design of the AWESOME. The antenna is an isosceles right triangle with an 18-meter base and a 9-meter height.

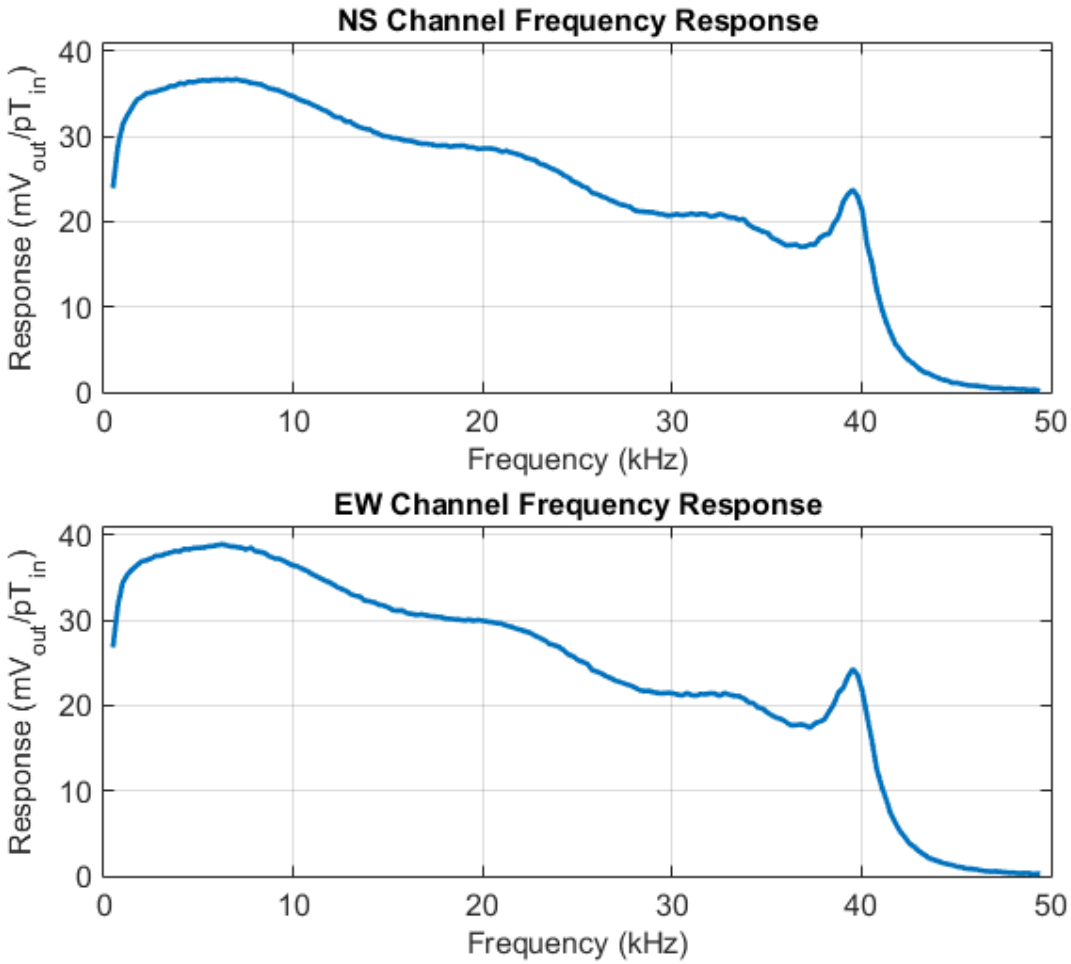

Figure 3: Frequency response of both channels of the receiver at Palmer Station, Antarctica.

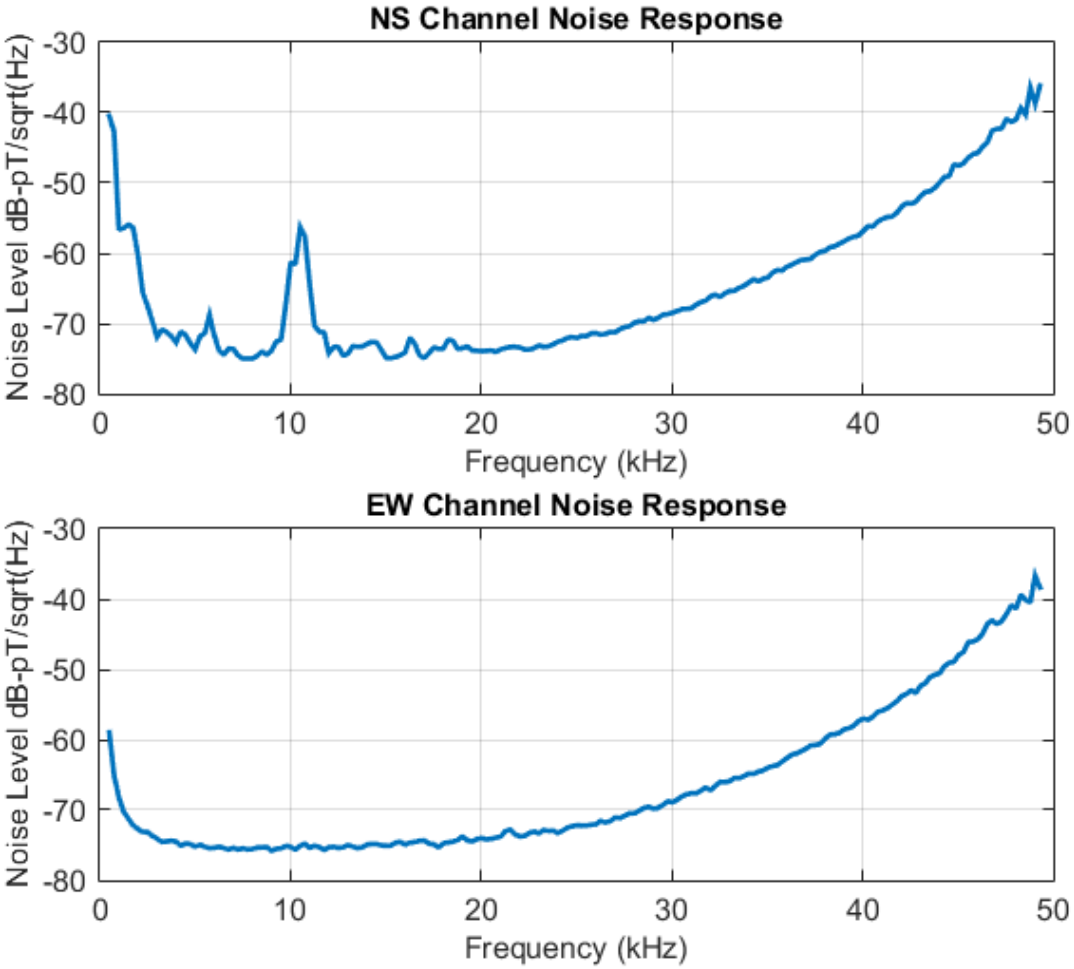

Figure 4: Noise response of both channels of the receiver at Palmer Station, Antarctica.

It was continuously operating during several large solar flares with broadly distributed lightning over South America and the Caribbean throughout the flare time period. This allows the consideration of sferic features both spatially and temporally.

2.2 GLD360 Geolocated Lightning Data

Lightning location data from the GLD360 network operated by Vaisala Inc. is utilized in this work. GLD360 is a globally distributed network of VLF receivers that together geolocate lightning globally. GLD360 uses primarily time of arrival to geolocate lightning, but also uses the sferic shape to provide a rough distance estimate,

which greatly boosts the detection efficiency of the network to ∼70%. The network calculates an initial guess for the location by using a cross-correlation of an expected distance-waveform bank on each receiver that detected the stroke. The network locates lightning with an industry best for timing and distance estimate (1−4 km), as well as detection (70%). GLD360 also reports the peak current and polarity of each stroke. For further information on the operating principles of GLD360, the reader is referred to *Said et al.* [2010]. A typical day of geolocated lightning strokes over the Americas is shown in Figure 5.

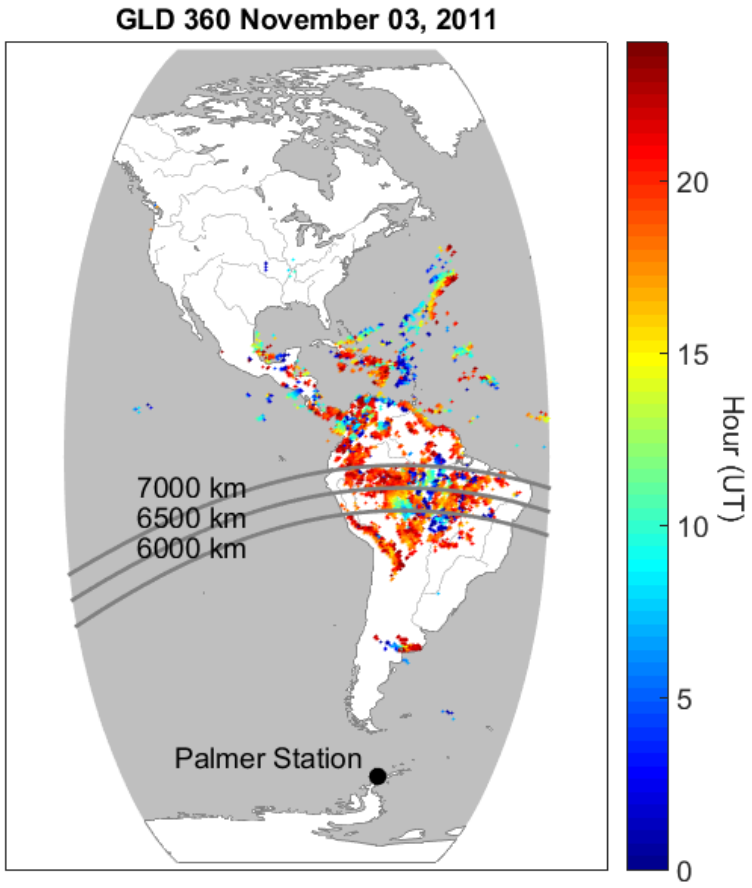

Figure 5: A typical distribution of geolocated lightning data. The distance labels are shown measuring distance from Palmer Station, Antarctica, the source of VLF broadband data used in this thesis. The colors show the time of the day the particular stroke took place.

The sferic waveform changes as a function of distance, but the waveform shape is also sensitive to the current incident x-ray flux. Although it is known that solar flares affect VLF propagation, the scope of the spatial, timing, and spectrum information as a function of x-ray flux is not yet characterized.

In order to validate the use of GLD360 during solar flares, we must quantify the effect of solar flares on geolocation. GLD360 is especially prone to errors arising during a solar flare disturbance since it uses the sferic waveform in its algorithm, but uses sferic shape estimates under typical conditions. In order to determine the effect of x-ray flux on the performance of the network, GLD360 performance is compared to the National Lightning Detection Network (NLDN), another network operated by Vaisala Inc. that locates lightning in the US based on the ground wave of lightning only. The ground wave does not reflect off of the ionosphere, and therefore is not sensitive to solar x-ray flares. Figure 6 shows the error of GLD360 as compared to NLDN both before and during a solar flare. It is observed that solar flares introduce a timing error on the order of 10 μs represented by an offset in the distribution, but it does not significantly affect the distance estimate provided by GLD360.

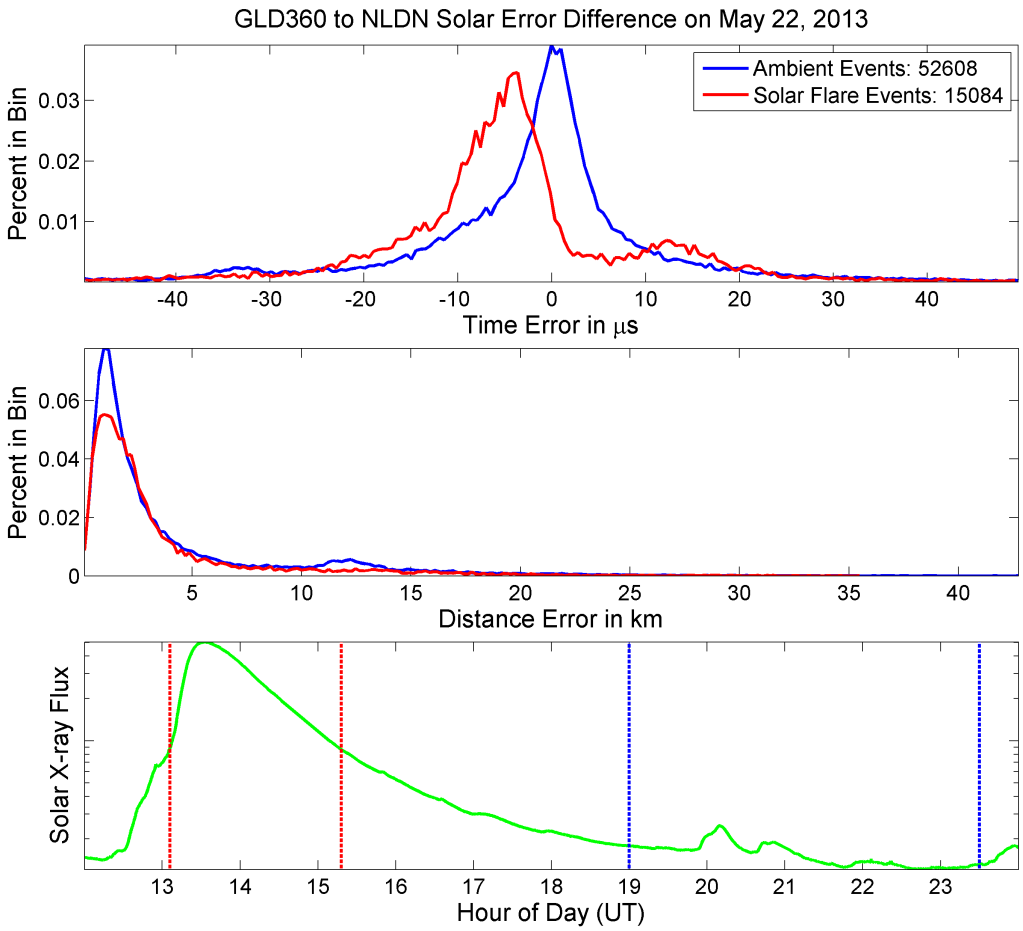

Figure 6: Error distribution of GLD360 compared to NLDN both during a flare and during ambient conditions. The red plot in the top panel is the difference between the time of the stroke in GLD360 and in NLDN during the solar flare, occurring between the red dashed lines on the bottom panel. Similarly, the blue line describes the same error before the flare during ambient conditions. The blue and red lines in the second panel describe the distance error calculated the same way, but measuring the distance error.

In addition to the timing bias of lightning geolocation in GLD360 that occurs during a solar flare, the distribution indicates that there will be significant jitter from sferic to sferic due to network error. This error is the dominant source of jitter in sferics seen later in the data, especially in Figure 17.

2.3 GOES Satellite X-ray Data

The National Oceanic and Atmospheric Administration (NOAA) operate a satellite called the Geostationary Operational Environmental Satellite (GOES). This satellite continuously monitors many solar emissions, including x-rays. We utilize these data to determine the onset of solar flares.

CHAPTER III

PROCESSING BROADBAND SFERICS

With perfect measurements and knowledge of the effective VLF source location, sferics from the same storm under the same ionospheric conditions should arrive at precisely the same time at the receiver. In reality, sferic arrival times vary from each other due to several factors. The source current emitted from the lightning strokes varies, for instance, as well as the length and shape of the lightning channel. These are collectively known as source effects, and are discussed in greater detail later.

There are, in addition, significant measurement errors. Although the absolute timing of both the GLD360 and Palmer Station VLF receivers are accurate to 100 ns, there are geolocation errors in both distance and time error that may then be different during solar flares or other ionospheric disturbances. These errors arise from the uncertainty of using a sferic that is hundreds of μs long to determine the arrival time. Additionally, at the receiver, noise, scattering, or multiple sferics arriving the same time are examples of non-ideal effects that cause errors in the sferic. An example of what sferics look like from a single storm with minimal processing is shown in Figure 7, with the corresponding locations shown on a map in Figure 8. Each sferic is time-adjusted using the GLD360 stroke time, so that 0 corresponds to the stroke time plus the propagation delay assuming propagation at the speed of light. In reality, sferics propagate slightly slower than the speed of light, but there is significant jitter in the arrival times of the sferics which under ideal conditions should not be present. Importantly, this jitter makes it difficult to immediately calculate an average sferic for this time period, which would otherwise allow a very clean measurement which can later be compared to a theoretical model.

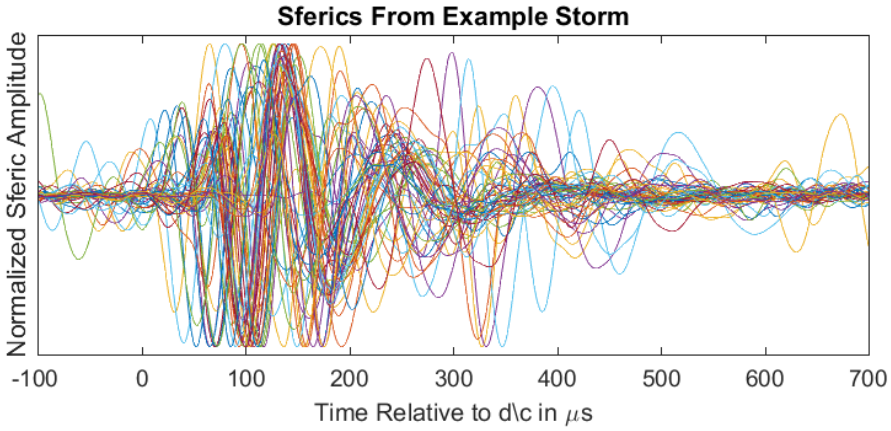

Figure 7: Sferics plotted together during an example storm with quiet solar conditions. Sferics are normalized by peak magnetic field and the sign of peak current.

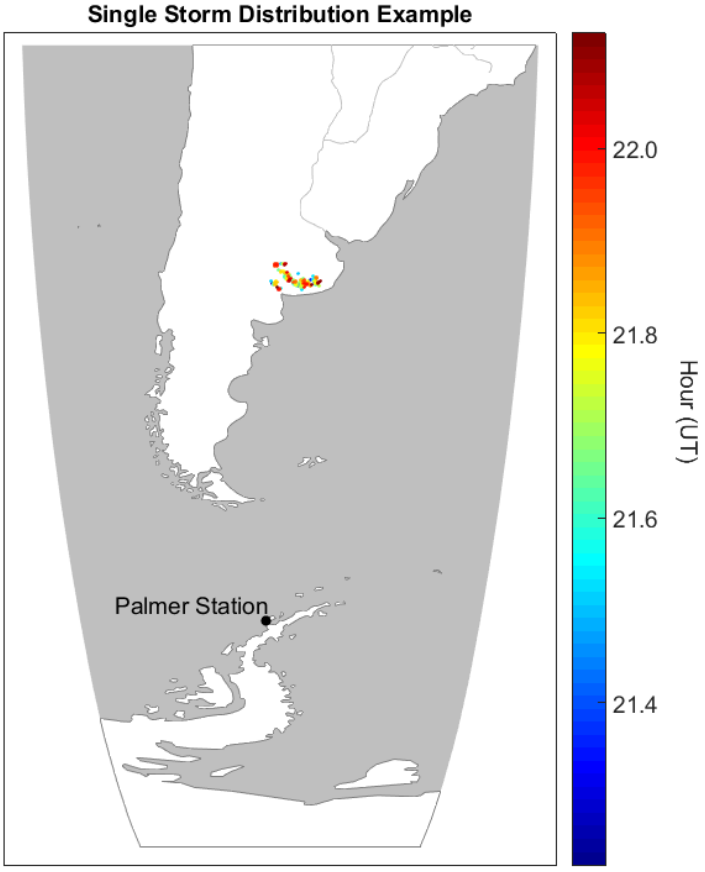

Figure 8: Map of lightning locations during a storm. Time of stroke occurrence is shown using color.

Although the sferics displayed occurred in confined area with similar atmospheric conditions and around the same time the sferics arrive at very different times from each other (jitter). In this section, we describe techniques to process the raw data and mitigate errors such as the jitter, to yield high fidelity sferics. A block diagram of all of the processing steps described in this thesis are shown in Figure 9.

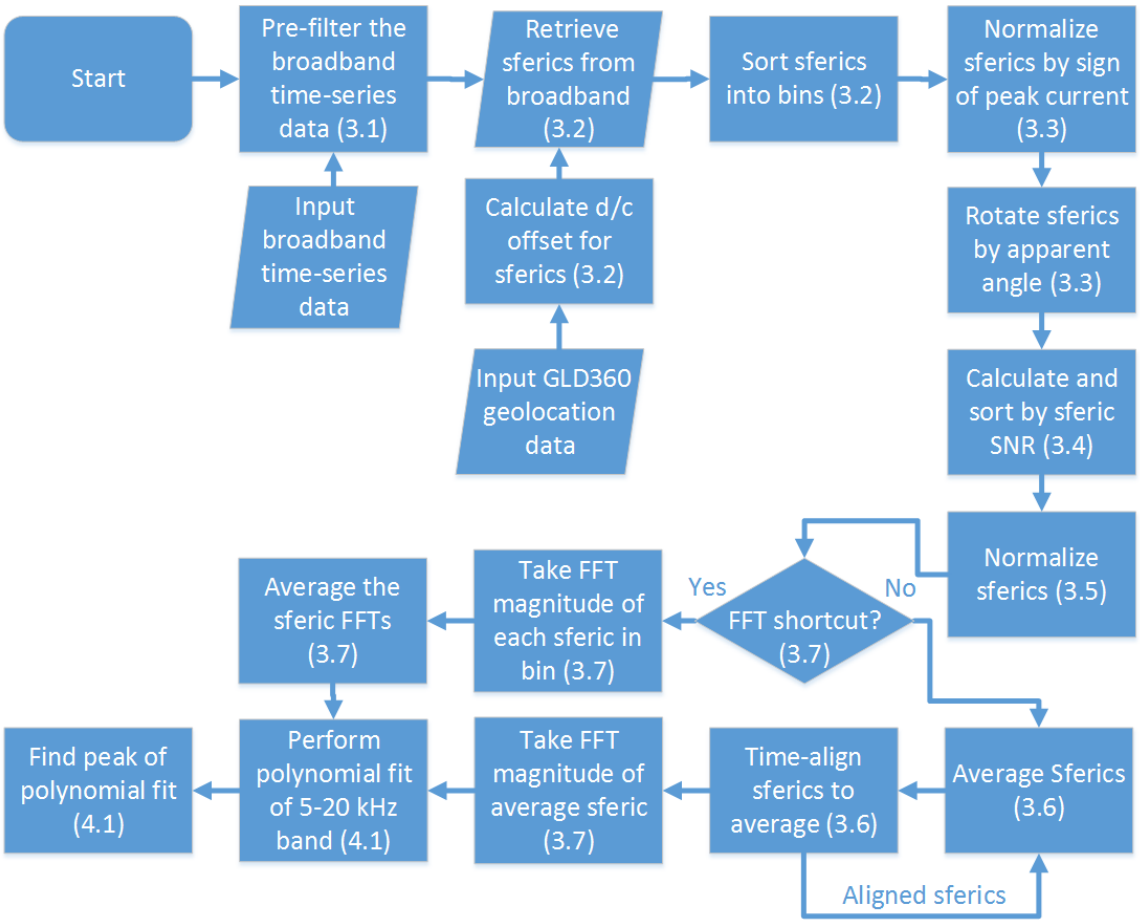

Figure 9: Block diagram of the processing steps described in this work. The section which describes the step is referenced in parenthesis.

3.1 Filtering Broadband Data

Before any processing begins, the data are filtered to remove unwanted signals. For instance, a number of navies operate VLF transmitters for communication with submerged submarines. These transmitter signals, like sferics, travel to global distances

with low attenuation. Therefore at the Palmer Station VLF receiver, many of these signals are present and strong. We pre-filter for all of the visible transmitters shown in Table 1. These transmitters broadcast with a very narrow-band signal, and are therefore called 'narrowband' signals. We therefore apply zero phase notch filters to the data (Orders N = 2-8, Quality Q = 40-300; values depending on received transmitter strength) in order to eliminate the interference without losing much information from the broadband sferic.

Table 1: Transmitters Receivable by Palmer

Location of Transmitter	Call Sign	Frequency (kHz)
Rosnay, France	HWU	18.3
Anthorn, UK	GBZ	19.6
Lualuahei, HI	NPM	21.4
Rhauderfehn, Germany	DHO	23.4
Cutler, ME	NAA	24.0
Jim Creek, WA	NLK	24.8
La Moure, ND	NML	25.2
Grindavik, Iceland	NRK	37.5
Aguada, Puerto Rico	NAU	40.8

When considering time-series data, filtering drastically improves the sferic measurement, enabling many of the processing techniques we will describe later. Figure 10 shows the effect of filtering on Palmer broadband data in both frequency and time. The Signal to Noise Ratio (SNR) of the sferics are drastically improved after the filtering process, as demonstrated by the top two panels.

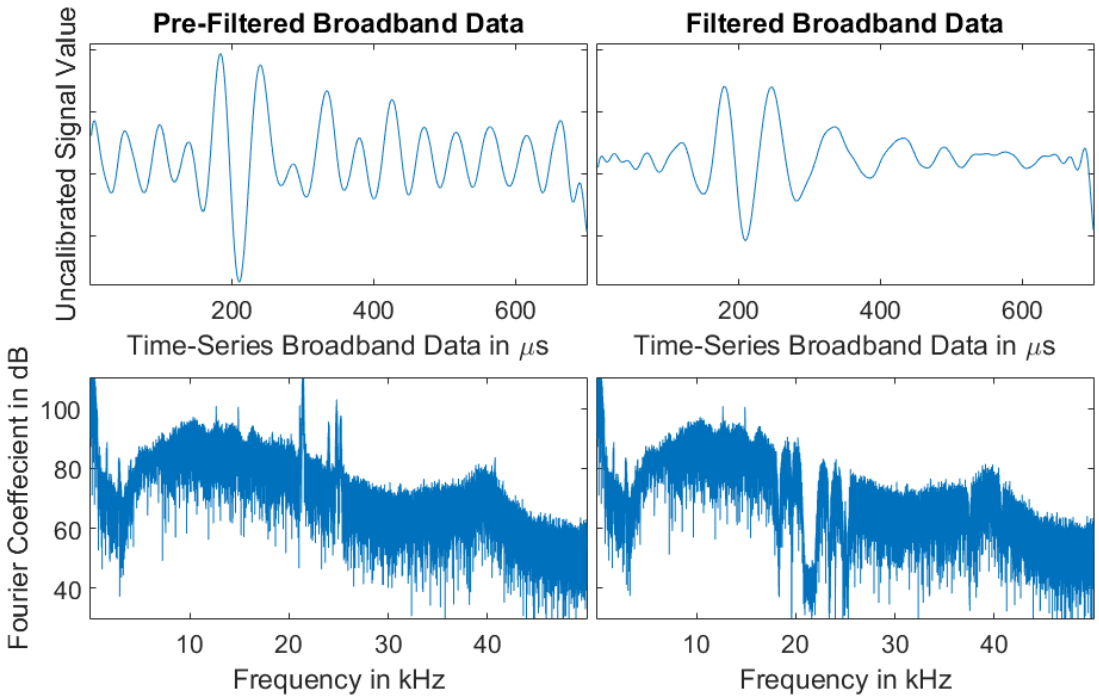

Figure 10: An example of broadband data filtering and its results. The left two panels are the pre-filtered data contrasted to the right panels with filtered data.

3.2 Sferic Retrieval and Binning

Since the VLF time-series data are continuous, we need to locate sferics corresponding to the lightning events reported by GLD360 in the data. Starting with the known time and location of each lightning stroke from GLD360, we calculate the expected arrival time at Palmer Station. The slightly non-spherical nature of the Earth is taken into account, in order to calculate the distance from source to receiver along the ground. The propagation speed is assumed to be the speed of light, c. The expected arrival time is then taken to be the lightning stroke time plus the propagation delay. This propagation-adjusted time is referred to as the 'd/c'. We retrieve each sferic in this manner.

The speed of light arrival time (d/c) is used as the starting point of the sferic. In reality however, the effective group delay varies by frequency but is slightly slower

than the speed of light, so the start of the sferic is typically slightly delayed from this reference point. We observe empirically that most of the sferic energy is contained in the first 700 μs of the sferic.

Sferics are sorted by time, distance, and arrival angle. Within each bin, we assume similar propagation conditions. This implies that apart from source effects, jitter, and measurement error the received sferics should be nearly identical. These sferics can therefore be averaged together to give a representative sferic with improved SNR. The space in which these sferics are constrained are hereafter referred to as a 'bin'.

3.3 Sferic Rotation

The arrival direction of sferics can in principle be determined by the ratio of the energy on each of the two channels. However, sferics propagate in a quasi-parallel plate waveguide, and contain a complicated mix of several modes. An introduction to parallel plate waveguides can be found in *Inan and Inan* [2000, chap. 4]. Ideally, modes will propagate parallel and perpendicular to the actual great-circle path. But the real waveguide creates a mix of transverse electric (TE) and transverse magnetic (TM) modes, so that, for instance, a sferic arriving from the north may have magnetic field components in both the north-south and east-west direction. Additionally, the two antennas may not be precisely orthogonal, which may skew the effective arrival angle further [*Said*, 2009, pg. 80].

The non-ideal effects between angle of arrival and maximum rotation angle can be seen in Figure 11. The distribution is not centered around zero degrees which demonstrates the effect of the non-ideal propagation. Furthermore, with different lightning days and even different sites, the distribution will vary. Because of these complications, we must determine an effective arrival angle empirically, instead of using the lightning location to assume the effective arrival angle.

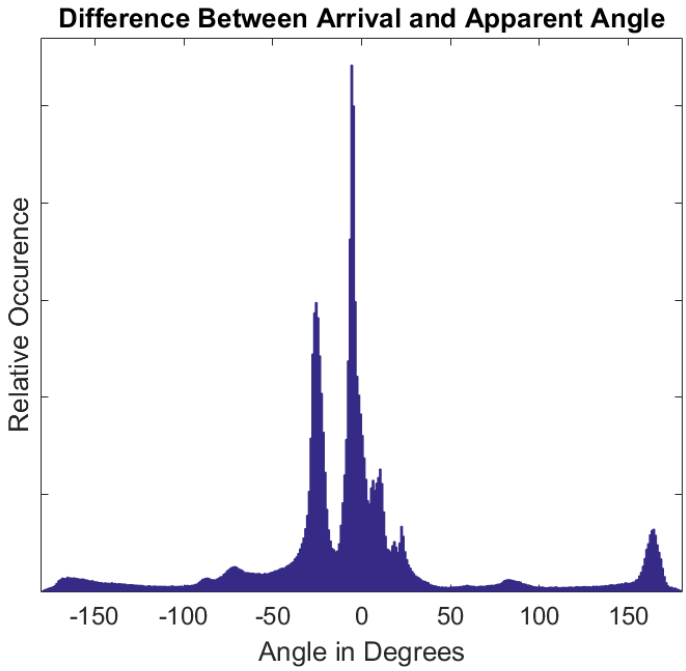

Figure 11: Difference between the effective arrival angle and the actual arrival angle.

Before determining the effective arrival angle, we normalize each channel by the sign of the peak current as estimated by GLD360. Additionally, we resample the data to 1 MHz for better granularity with time-series processing. We then empirically calculate the effective rotation angle that will result in the maximum amount of energy on one channel. This is hereafter known as the high-SNR channel. The rest of the signal energy will be deposited on the second channel hereafter known as the low-SNR channel. An example of a sferic rotated is shown in Figure 12.

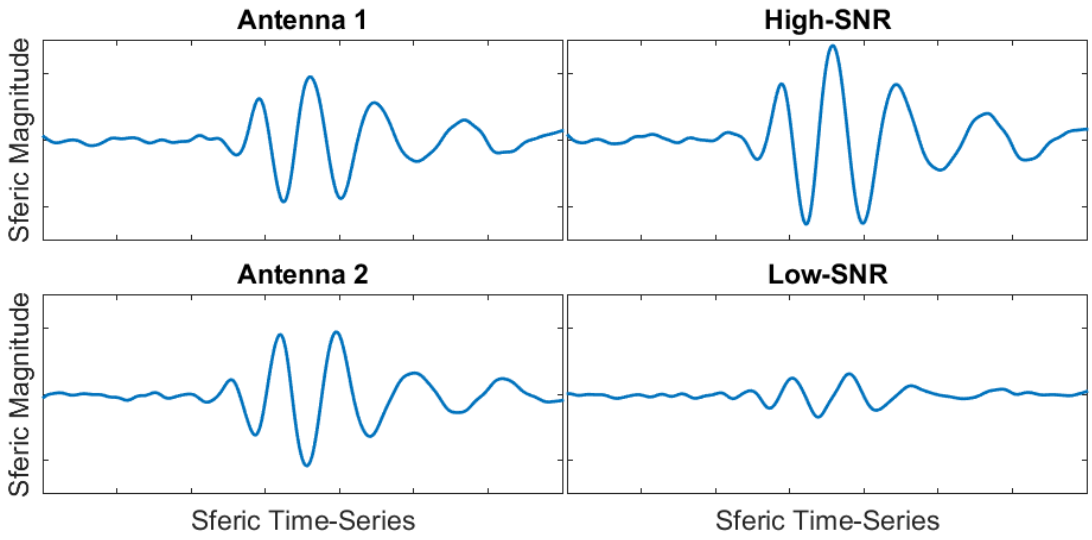

Figure 12: A sferic recorded on both channels at Palmer Station, Antarctica before and after rotation.

The maximum is found using a traditional gradient descent algorithm. The algorithm proceeds by taking the gradient of the function, and moving toward the minimum, or 'descending'. When the gradient is found to be zero, the minimum is returned. In this case, gradient descent is applied to the energy ratio between the channels. The shape of the energy ratio between the channels is sinusoidal, so we can guarantee that the algorithm is stable and converges to the global extremum.

3.4 SNR Cutoff

In order to accurately utilize sferics, we need to isolate only those that are significantly stronger than the ambient noise at the receiver. Higher source peak current generates stronger electromagnetic radiation and therefore stronger sferics. However, the SNR also varies with distance and ionospheric condition, so the peak current on its own is not a proxy for SNR. Figure 13 shows the SNR vs. peak current magnitude for sferics of a similar propagation path. There is no obvious trend when considering the data, therefore, we use a SNR measurement as the measure of sferic quality.

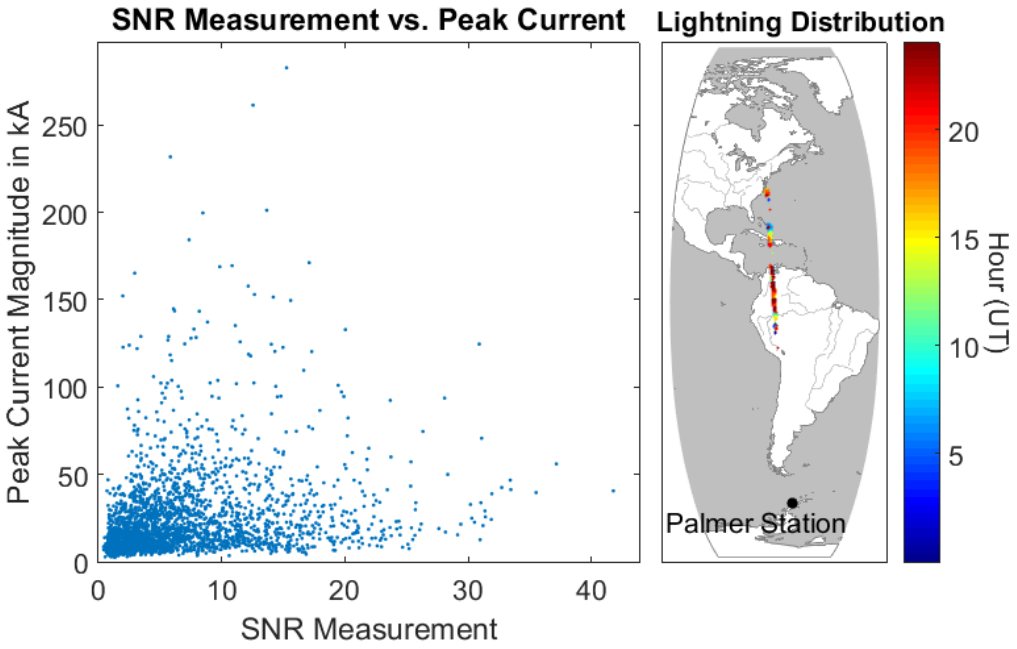

Figure 13: Events are shown for 2011/09/24. All events shown are for arrival angles between 350 and 351 degrees in order to compare similar propagation paths.

We therefore directly measure sferic SNR, defining SNR as the measured smoothed signal peak divided by the rms noise value. We apply a SNR cutoff of 5 and only sferics at or above this cutoff are utilized. Sferics are retrieved from the broadband data in a window longer than the sferic, with baseline noise before and after the sferic. The sferic used to measure SNR is filtered and rotated before the measurement.

The effective group delay varies by frequency but is slightly slower than the speed of light, so the start of the sferic is typically slightly delayed from the d/c time. We observe empirically that most of the sferic energy is contained in the first 700 μs of the sferic. In Figure 14, the portion before the d/c, and after d/c time plus 700 μs are the noise portions of the signal.

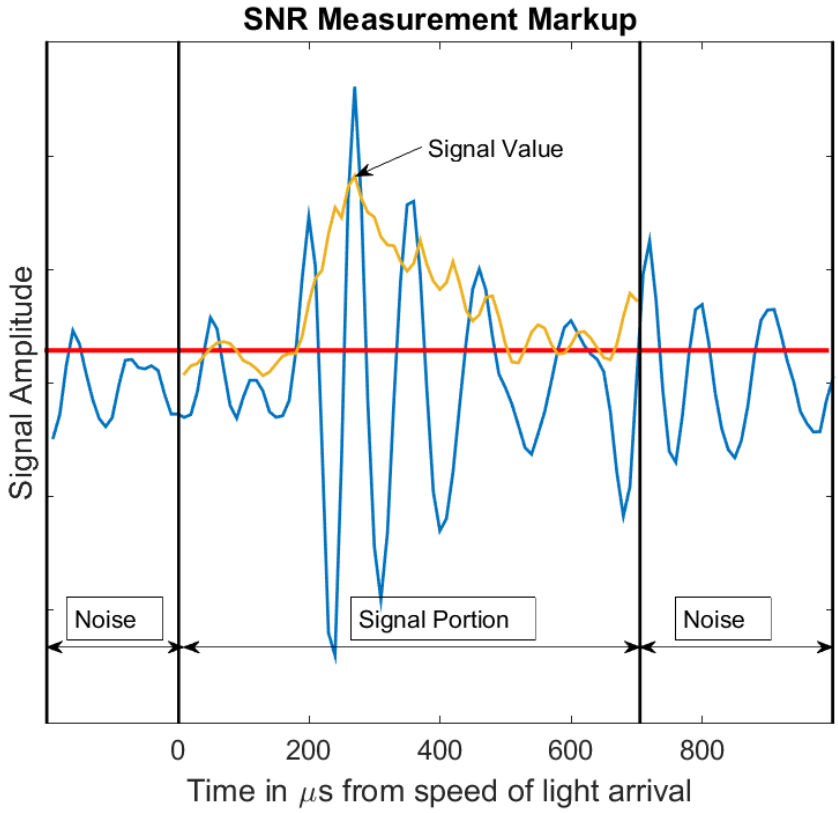

Figure 14: Markup of the measurement of the SNR of a sferic. The first and last portion are the noise portions, in between is the signal portion.

The noise portions are concatenated and the rms value is taken as the noise value. A smoothing filter is applied to the signal and the peak of the smoothing filter with a window size of 4 is the signal value.

3.5 Normalizing Sferics

Since our goal is to average a number of sferics, we normalize them by their peak signal value so that they count equally in the averaging. Many sferics are averaged to improve the representative sferic of that bin. For a similar path, peak current alone is not a proxy for received signal strength as seen in 15.

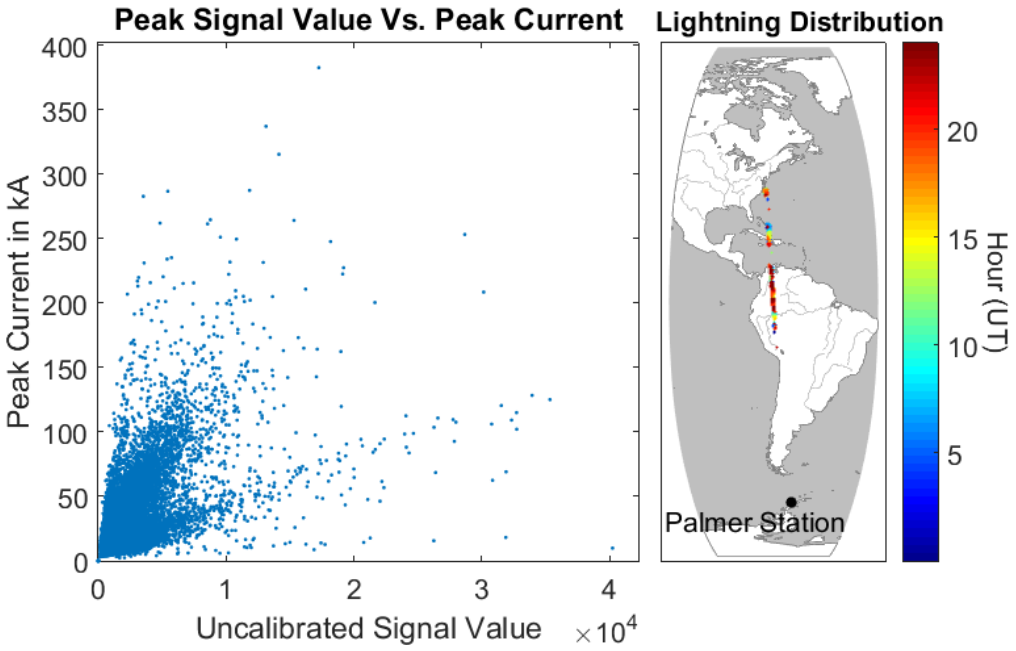

Figure 15: Peak signal values vs. peak current at Palmer Station. Events are shown for 2011/09/24. These events are all filtered to have at least a SNR of 5. All events shown are for arrival angles between 350 and 351 degrees.

There does not appear to be one dominant trend in the data, therefore, we use the measured signal value as the normalization constant.

3.6 Recursive Time-Alignment and Averaging

As discussed, we average sferics within the same bin in order to create an accurate representative sferic. However, the significant and often unpredictable jitter from sferic to sferic is problematic. Sferics do not align in time and the averaged time signal is distorted. To combat this, we time-align the sferics to the initial raw average, then take a new average of the aligned sferics. By using the improved average as a starting point, a recursive alignment will continue to improve the SNR of the representative average.

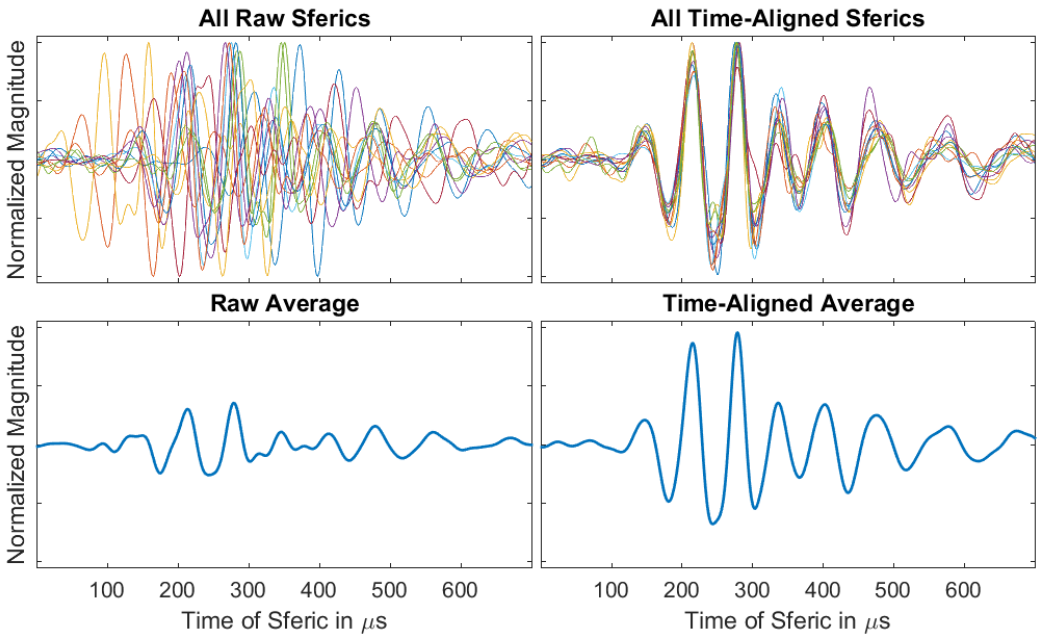

Figure 16: Results of time-alignment of received sferics. The x-axis of every plot is the time of the sferic after d/c arrival in μs.

Even for high SNR sferics, the jitter is too great to result in anything but a distorted average. However, we greatly improve the sferic average with time-alignment. This technique allows the recovery of signals that would be artificially lost because of the jitter in the d/c estimate.

3.7 Feature Extraction and Consideration

After we time-align the sferics the averaged sferics have greatly improved SNR. However, due to error distribution in GLD360, we still observe significant jitter in the d/c time from bin-to-bin. This is clearly seen in Figure 17.

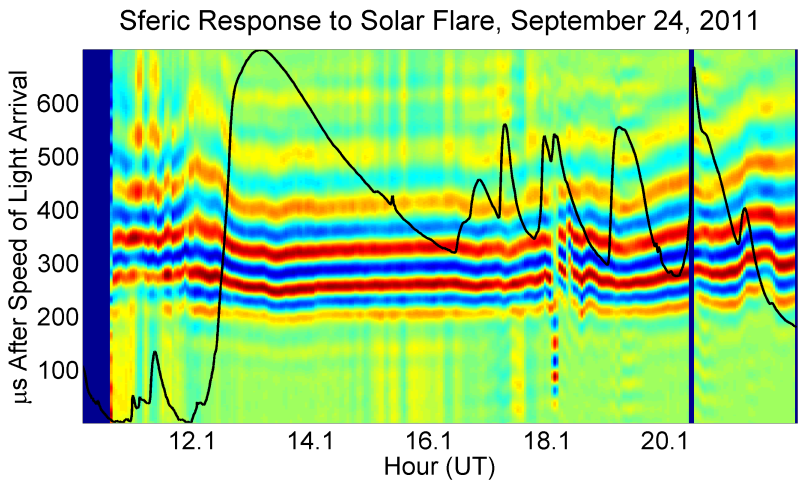

Figure 17: Plot of sferics during the day throughout several solar flares. Each column represents the processed sferic from one bin at a constant time of day. Red are positive values, and blue are negative values. The solar x-ray flux is overlayed on the plot in black. The dark blue section on the left corresponds to missing data.

There are many time shifts and disturbances during solar flares as explained by the network-biased jitter. However, there is also significant jitter in the day before the first solar flare occurs. Without correcting for this, comparing sferic features changes from bin-to-bin is difficult or impossible.

Therefore, we need to separate the sferic information from inherent jitter. Further, in order to be able to see how sferics change, it is convenient to be able to consider a smaller set of data than the entire time-series. Sferic shape and group velocity changes as a function of distance. However, for the sferic propagation distances to Palmer, there are peaks in the sferic that are always present despite jitter. These are labeled 'Peak 1' and 'Peak 2' in Figure 18.

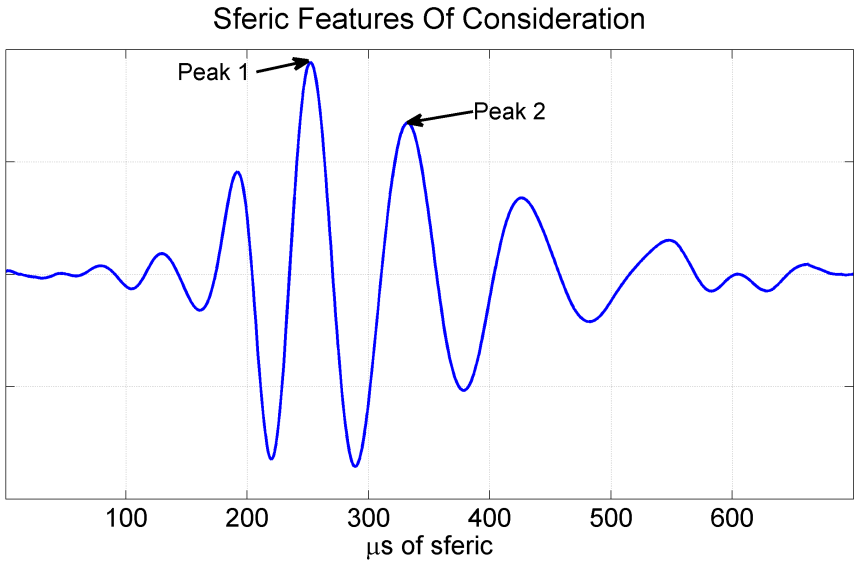

Figure 18: Illustration of features considered in the initial work described below. This waveform depicts a 'typical' sferic at large distances (>3000km) with the preliminary features considered marked up.

The results of the delay of Peak 1 and 2 are extracted and the time-delay between them is considered as a function of time and distance. These results are shown in Figure 19.

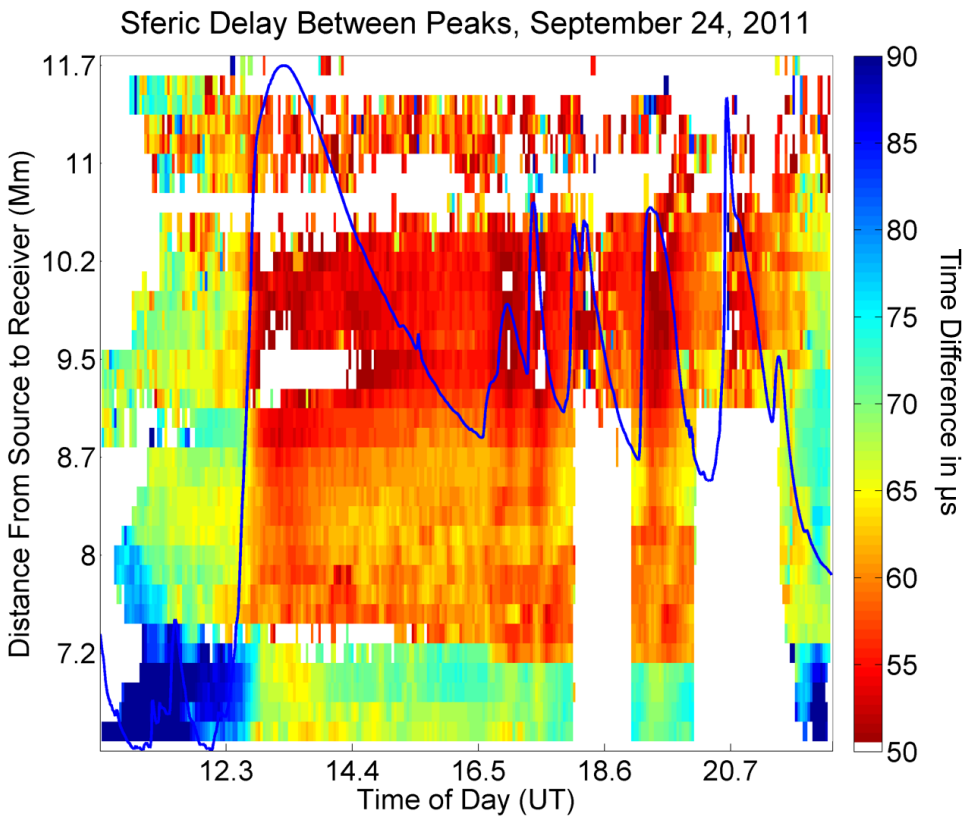

Figure 19: The color represents the delay between the first and second peak as depicted in Figure 18. Overlaid on the plot is solar x-ray flux during this time range. The white cells represent missing data.

After time-aligning sferics and considering changing features within a single waveform, some trends are visible in the data. There are significant changes in delay between the first and second peak correlating in time perfectly to solar flares. In addition, the effect on the time difference of the sferic varies with distance. Furthermore, there are abrupt and unexpected changes in time difference along distances. This probably indicates a failure to correctly extract the features of the sferic. This problem is complicated due to bin-to-bin jitter. It especially becomes difficult since the position of the peaks considered vary as a function of distance, and often-times unpredictably, as during a solar flare.

Since the Fast Fourier Transform (FFT) magnitude does not depend on phase or start point of the signal, it is a good candidate to remove this jitter problem. Using the FFT removes phase information from the sferic that cannot be recovered. The left panel of Figure 20 shows several FFTs of bins at the same location at different times. These FFTs correlate very well from around 5-20 kHz. However, outside of this frequency range, the match integrity degrades significantly. The frequency variance >20 kHz could be explained by source effects. Lightning moves in discrete steps to form the lightning channel on the order of hundreds of meters [*Rakov and Uman*, 2003]. As frequency increases, it is expected that the stepping and jagged shape of the lightning channel would have a greater impact since smaller wavelengths are comparable to the step length.

However, rather than time-aligning, and then comparing the FFT from time-based techniques, the FFT is taken of each individual sferic after rotation and normalization, with the average taken of all the sferic FFTs in the bin. When comparing the average FFT from bin-to-bin, this technique shows reduction in variability of low frequency and high frequency content, allowing for more stable analysis.

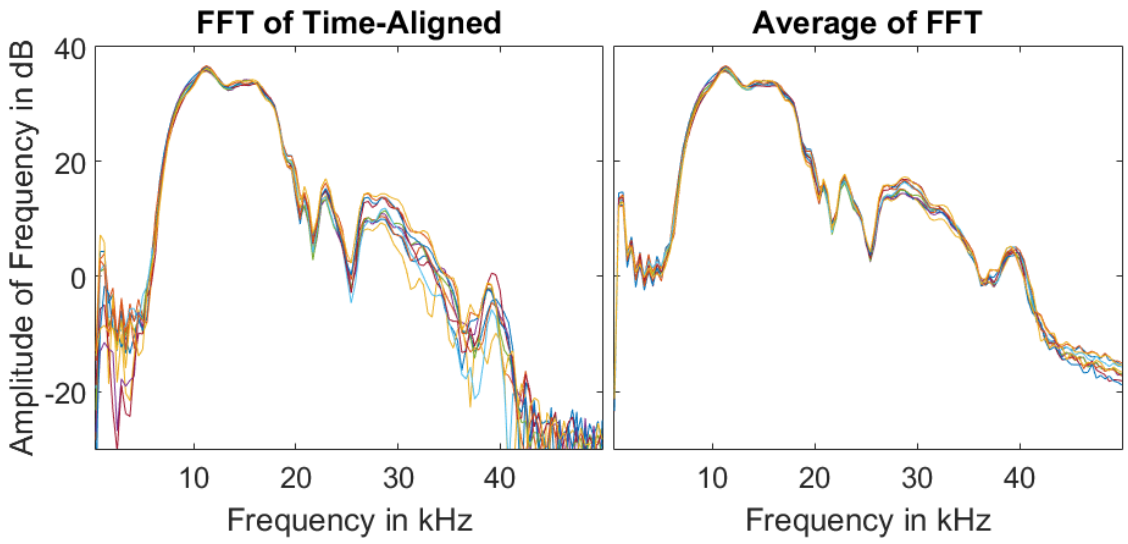

Figure 20: FFT Alignment Shortcut. Each color line is the FFT of another sferic of a similar location and time of day.

CHAPTER IV

RESULTS AND DISCUSSION

The data have been processed and sorted for distance from the receiver, angle of arrival, and time of day. We have plotted only bins which have at least 5 high-SNR sferics in them.

Because of the broad occurrence of lightning, ionospheric disturbances may be detectable over a wide range of space and time. Both day and nighttime propagation effects will affect the sferic propagation. Figure 21 shows the propagation paths as well as the night and day spread along those paths at midnight UT.

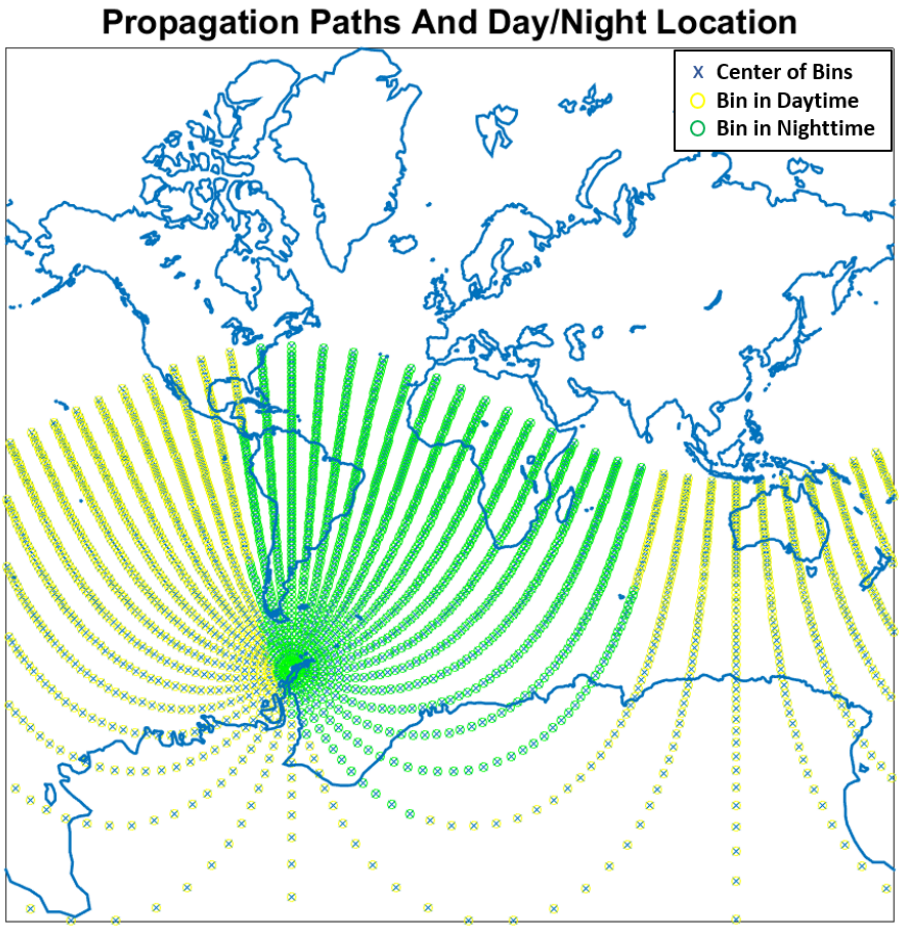

Figure 21: Sketch of coverage of sferic paths from Palmer. The blue 'x' marks are the center of the bins and the representative location of the sferics closest to their location.

Due to the efficient propagation of sferics, much of the southern hemisphere ionosphere can be indirectly sensed using the processed sferics at a single receiver. These sferics can be used to sense the ionosphere during stable conditions as well as disturbances such as solar flares or other disturbances.

4.1 Frequency Features

Each sferic contains at least 70 data points to consider. The data set is too large to consider trends in the change of the sorting parameters as is. Therefore for this

section, change in frequency features are considered because of its stability.

We use the sferic band from 5-20 kHz since it has been demonstrated to be the most stable portion. We apply a third order polynomial to characterize the frequency content of the averaged sferics in this range. Figure 22 shows a waveform and the polynomial fit portion superimposed.

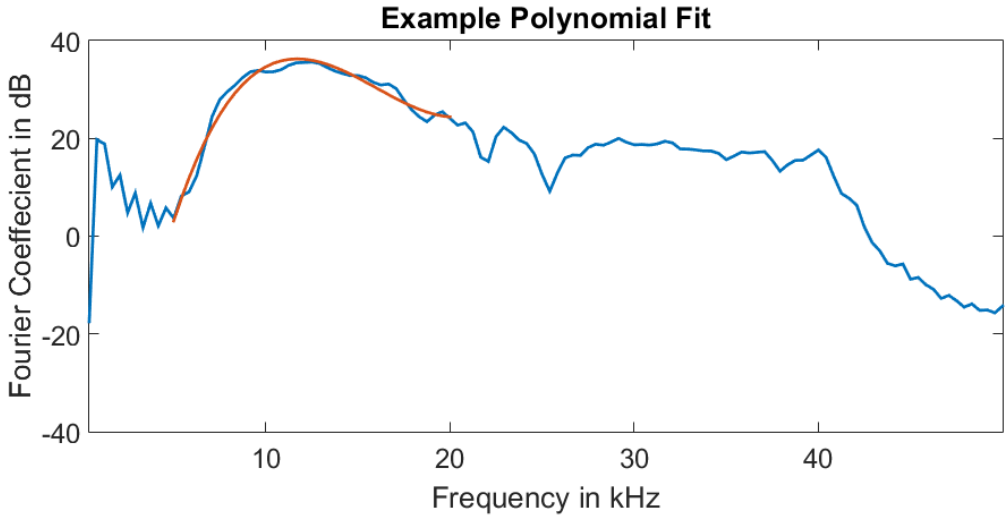

Figure 22: Figure of a polynomial fit and FFT example used in these results. The blue line is the entire FFT, while the red line is the third order polynomial fit.

For most sferics, a simple third order polynomial seems to capture the bulk of unique features of its FFT magnitude. For a third order fit the data set has been reduced to 4 coefficients. To further reduce the data set to a form that can be considered with reasonable difficulty, the peak polynomial frequency is used as the feature in the rest of this analysis.

4.2 Discussion

The received sferics spectrum vary due to many factors. Due to varying ionization conditions, solar zenith angle and day or nighttime conditions will affect propagation. Even under an assumed uniform ionosphere, the Earth's magnetic field will cause an

angle-dependent propagation attenuation [*Hutchins et al.*, 2013]. Because of this fact, information will be shown with a fixed angle range, displaying the sferic feature vs. time vs. distance. The sferic shape itself also changes as a function of propagation distance. An expected waveform vs. distance plot is shown in Figure 23, courtesy of Morris Cohen.

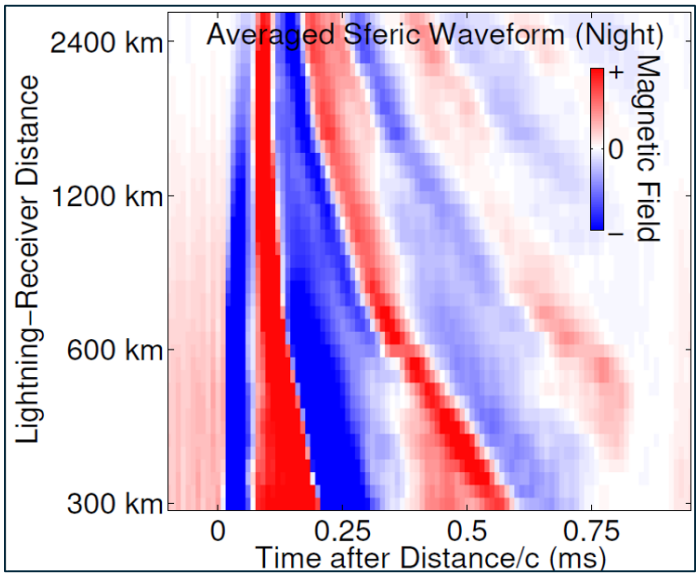

Figure 23: Figure of the expected sferic waveform vs. distance. Each row contains a single sferic at a set distance.

As the sferic propagation distance increases the waveform is compressed. Furthermore, the first portion of the sferic that arrives attenuates faster than the rest of the signal such that it is only weakly present at 2500 km. In other words, the group velocity of the sferic decreases with distance.

Binning sferics by narrow location and time bins may have the effect of distinguishing localized disturbances only visible on short spatial and time scales. Figure 24 shows a quiet solar day a fixed angle from Palmer Station, Antarctica.

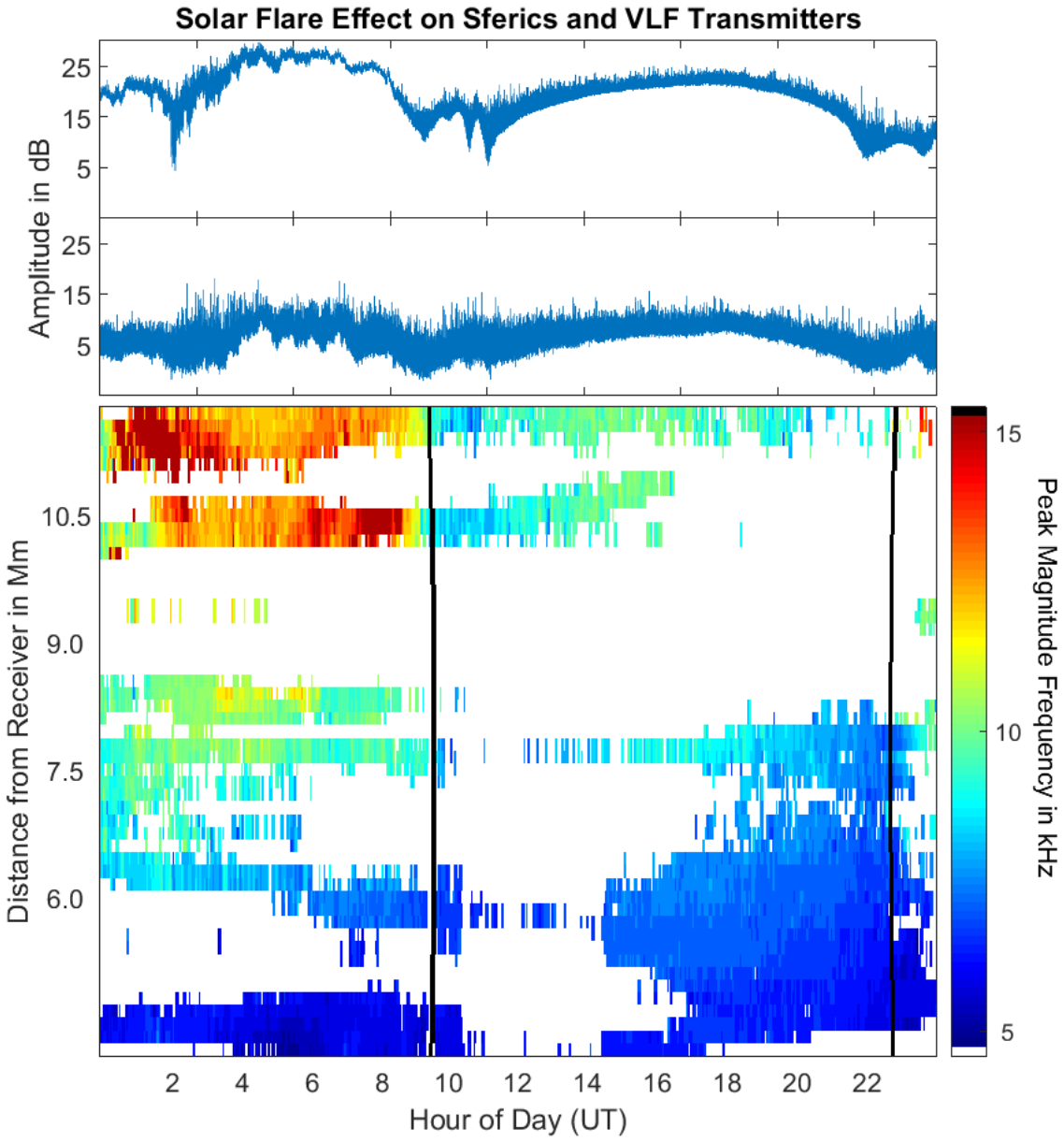

Figure 24: Signals propagating in the Earth-ionosphere waveguide on 01/09/2011 to Palmer Station, Antarctica during a quiet solar day. The top two plots are the amplitudes of both channels of NAA, a VLF transmitter described in Table 1. All three plots are shown for the entire day. The bottom plot shows the frequency with the peak magnitude. The black lines represent the day-night terminator line, with daytime in-between the lines, and nighttime outside of them. White cells represent missing data.

For the peak frequency of sferics, there is a strong dependence on night vs. day propagation seen by the very different and distinct regions in night and day. The difference between the regions is smaller at closer distances to the receiver. During the daytime, the peak frequency evolves, which could be a function of solar zenith angle. During the nighttime, the changes are much more chaotic, which is consistent with other measures of the D-region of the ionosphere at night. This includes monitoring by using narrowband Navy VLF Transmitters.

VLF transmitters have a rich history of being used for monitoring and studying the ionosphere as discussed in Section 1.1. During the night, the amplitude is stronger, and also more variable than during the day. The transition between night and day introduces some more variability due to the hard transition between drastically different ionospheric conditions in day vs. night. This transition is known as the day-night terminator. During the day, the amplitude is more predictable, and the amplitude follows the solar zenith angle, with the peak correlating with the highest zenith angle sun. These results are consistent with the results shown with the study of VLF transmitters such as in *McRae and Thomson* [2000], but this method is limited by a single transmitter-receiver path at a single frequency. In contrast, sferics act as a VLF transmitter at many different frequencies with many different paths increasing their utility. VLF transmitters have also been used to study the ionosphere during solar flares. A very active solar day is now considered in Figure 25 contrasting VLF narrowband measurements with the peak sferic frequency.

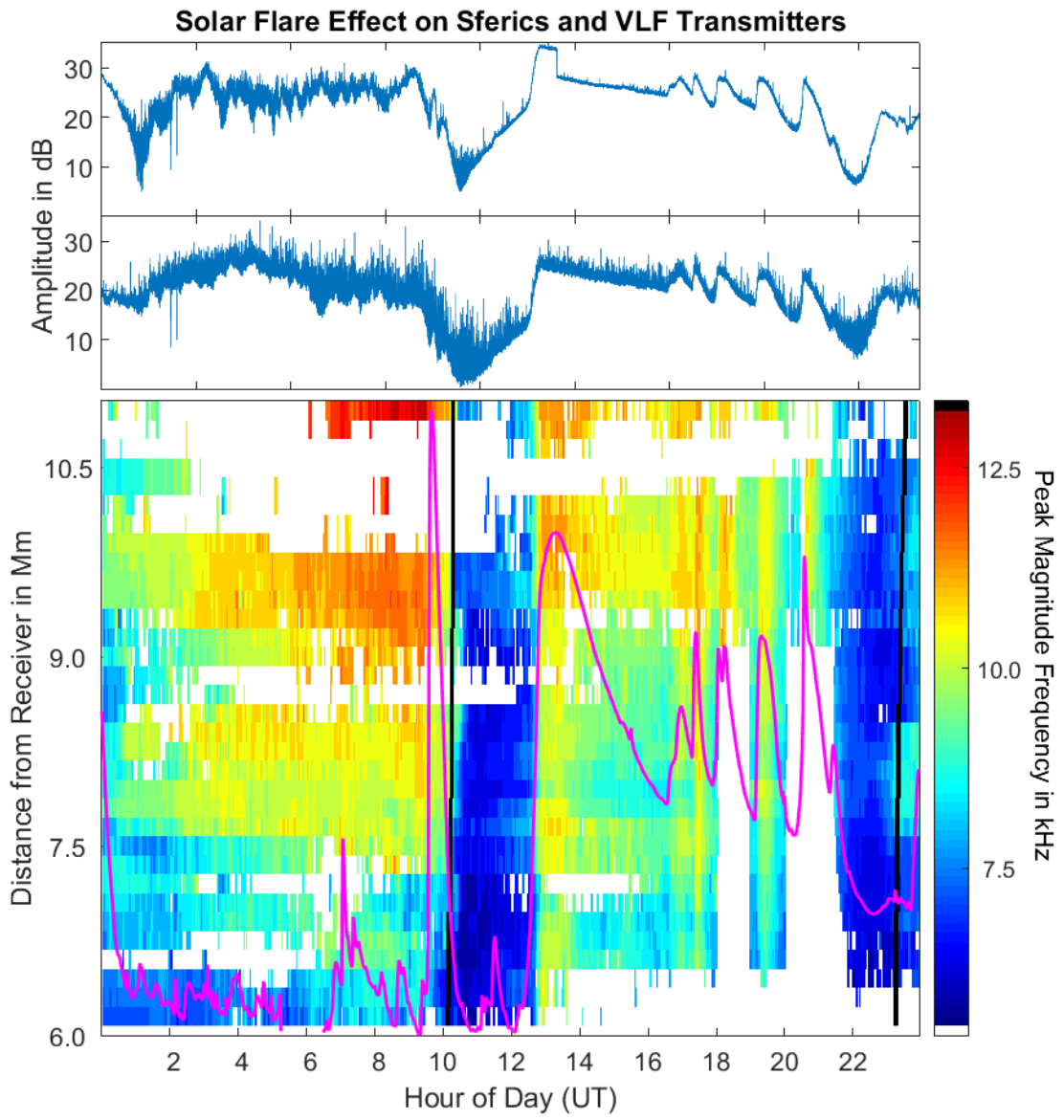

Figure 25: Signals propagating in the Earth-ionosphere waveguide on 01/09/2011 to Palmer Station, Antarctica during a very active solar day. The top two plots are the amplitudes of both channels of NAA, a VLF transmitter described in Table 1. All three plots are shown for the entire day. The bottom plot shows the frequency with the peak magnitude. The black lines represent the day-night terminator line, with daytime in-between the lines, and nighttime outside of them. The solar x-ray flux from GOES is overlaid on top of the plot in magenta. White cells represent missing data.

In addition to the strong dependence on both distance and night/day on the effects seen during the ambient day, the feature is also strongly affected by solar flux during the day. This agrees with the VLF transmitter measurements which are also perturbed during the solar flare. There is a strong solar flare that occurs during the night, but has no effect on the sferic feature, or on the transmitter amplitude. However, each of the several solar flares has an effect at all displayed distances. This frequency shift increases with greater propagation distances. The effect also relaxes quickly with diminishing solar flux.

As seen, the presented techniques have an ability to sense effects on the ionosphere on a great distance and time scale. Because of these facts, sferics are a powerful remote sensing tool. They can be used to sense the ionosphere on a greater space scale than single path transmitter-receiver measurements and greater time-scales than other methods.

Because this work focuses on ionospheric effects sensed indirectly through sferics, it is difficult to directly compare to other ionospheric measurements. Rocket-based measurements, are accurate, but too local to compare with confidence to VLF transmitter or sferic measurements, which measure average ionospheric parameters. Other measurements commonly used to study the ionosphere such as ionosondes or incoherent scatter radar, do not perform well on the D-region. This is because the D-region is very weakly ionized compared to the E and F regions and it is difficult to generate waves that reflect cleanly off of the D-region. Therefore, VLF and sferic methods are the best candidate for further study of the D-region of the ionosphere.

4.3 Conclusion

The objective for this work was to develop a technique to use broadband sferics to be able to sense the D-region of the ionosphere. This technique has been demonstrated to increase the SNR of sferics and mitigate jitter in the sferics. By using these highlighted

methods, the large dataset of sferics has been improved, allowing for greater utility when studying the ionosphere.

The techniques presented in this work have paved a way to use sferics broadly distributed in space and time to indirectly sense the ionosphere on both macroscopic and microscopic time and location scales. These methods have been implemented and demonstrated for both a quiet solar day, and a very active solar day. Some of the effects have been qualitatively discussed while many more effects are still in need of further investigation.

APPENDIX A

DEFINITIONS AND ACRONYMS

β

The Wait parameter describing the 'sharpness' or gradient of the electron density in the D-region of the ionosphere.

AWESOME

Atmospheric Weather Electromagnetic System for Observation, Modeling, and Education. The radio receiver revision after the receiver at Palmer Station, Antarctica that recorded the broadband time-series data for this work.

Bin

A window of location and time of day. Sferics are sorted by into bins, and then processing occurs within each bin.

Broadband

Time-series magnetic field data sampled by the pre-AWESOME instrument. Includes frequency information from about 1-50 kHz.

D-region

The portion of the ionosphere from around 70 to 85 km that reflects electromagnetic waves in the VLF and LF frequency bands.

d/c

Speed of light arrival time. 'd' is the distance of propagation, and 'c' is the speed of light. d divided by c yields a time.

Earth-Ionosphere Waveguide

The waveguide made up of the ionosphere and the Earth ground. This guides waves up to global distances by trapping electromagnetic energy between these two layers.

FDTD

Finite Difference Time Domain. Numerical method for computing propagation of electromagnetic fields.

FFT

Fast Fourier Transform. Used in this work to filter and consider spectrum changes of sferics vs. changing location and time scales.

GLD360

Network operated by Vaisala Inc. that geolocates lightning globally. It provides a location, time, and peak current estimate of the lightning stroke.

H′

The Wait parameter describing the 'effective reflection height,' or offset of the D-region from the ground.

Ionopshere

The portion of Earth's atmosphere from about 70 to 500 km that is ionized by galactic cosmic rays, x-rays, and Lyman-α radiation. This layer of the atmosphere is a plasma.

LEP

Lightning-Induced Electron Precipitation. Describes the interaction between VLF energy in space causing electrons to precipitate and be absorbed by the Earth's atmosphere.

LF

Low Frequency. The electromagnetic frequency band from 30-300 kHz.

LWPC

Longe Wave Propagation Capability. A model used to infer H′ and β from measured VLF signals.

Lyman-α

Spectral lines emitted from an electron state change in hydrogen from the second to the first discrete energy level. The emitted photons have a wavelength of 121.6 nm.

Narrowband

Referring to VLF transmitters operated by various Navies. These transmitters operate with a narrow frequency band.

NLDN

National Lightning Detection Network. A lightning location network operated by Vaisala Inc. that locates lightning strokes in the United States and the Caribbean.

Plasma

A state of matter in which gas is heavily ionized and the electrons are only weakly associated with their nucleus.

Sferic

The broadband signal generated by a lightning stroke. It will propagate to global distances with low attenuation guided by the Earth and the ionosphere.

Solar Flare

A sudden increase in radiation by the sun. Often marked by an optical flare on the surface of the sun.

VLF

Very Low Frequency. The electromagnetic band from 3-30 kHz.

Bibliography

Bilitza, D., and B. W. Reinisch, International reference ionosphere 2007: Improvements and new parameters, *Advances in Space Research*, *42*(4), 599–609, doi: 10.1016/j.asr.2007.07.048, 2008.

Cheng, Z., S. A. Cummer, D. N. Baker, and S. G. Kanekal, Nighttime d region electron density profile and variabilities inferred from broadband measurements using vlf radio emissions from lightning, *Journal of Geophysical Research*, *111*(A05302), doi: 10.1029/2005JA011308, 2006.

Cohen, M. B., U. S. Inan, and E. W. Paschal, Sensitive broadband elf/vlf radio reception with the awesome instrument, *IEEE Transactions on Geoscience and Remote Sensing*, *48*(1), 2010.

Cummer, S. A., U. S. Inan, and T. F. Bell, Ionospheric d region remote sensing using vlf radio atmospherics, *Radio Science*, *33*(6), 1781–1792, 1998.

Dahlgren, H., T. Sundberg, A. B. Collier, E. Koen, and S. Meyer, Solar flares detected by the new narrowband vlf receiver at sanae iv, *South African Journal of Science*, 2011.

Ferguson, J. A., Computer programs for assessment of long-wavelength radio communications, *Tech. Rep. 3030*, Space and Naval Warfare Systems Center, San Diego, 1998.

Friedrich, M., and K. M. Torkar, Firi: A semiempirical model of the lower ionosphere, *Journal of Geophysical Research*, *106*(A10), 21,409–21,418, doi: 10.1029/2001JA900070, 2001.

Grubor, D. P., D. M. Šulić, and V. Žigman, Classification of x-ray solar flares regarding their effects on the lower ionosphere electron density profile, *Annales Geophysicae*, *26*, 1731–1740, 2008.

Han, F., and S. A. Cummer, Midlatitude daytime d region ionosphere variations measured from radio atmospherics, *Journal of Geophysical Research*, *115*(A103314), doi:10.1029/2010JA015715, 2010a.

Han, F., and S. A. Cummer, Midlatitude nighttime d region ionosphere variability on hourly and monthly time scales, *Journal of Geophysical Research*, *115*(A09323), doi:10.1029/2010JA015437, 2010b.

Han, F., S. A. Cummer, J. Li, and G. Lu, Daytime ionospheric d region sharpness derived from vlf radio atmospherics, *Journal of Geophysical Research*, *116*(A05314), doi:10.1029/2010JA016299, 2011.

Helliwell, R. A., J. P. Katsufrakis, and M. L. Trimpi, Whistler-induced amplitude perturbation in vlf propagation, *Journal of Geophysical Research*, *78*(22), 4679–4688, 1973.

Hutchins, M. L., A. R. Jacobson, R. H. Holzworth, and J. B. Brundell, Azimuthal dependence of vlf propagation, *Journal of Geophysical Research*, *118*(9), 5808–5812, doi:10.1002/jgra.50533, 2013.

Inan, U. S., and A. Z. Inan, *Electromagnetic Waves*, Prentice Hall, 2000.

Inan, U. S., T. F. Bell, and J. V. Rodriguez, Heating and ionization of the lower ionosphere by lightning, *Geophysical Research Letters*, *18*(4), 705–708, 1991.

Kintner, P. M., R. Brittain, M. C. Kelley, D. L. Carpenter, and M. J. Rycroft, In situ measurements of transionospheric vlf wave injection, *Journal of Geophysical Research*, *88*(A9), 7065–7073, doi:10.1029/JA088iA09p0706, 1983.

Kockarts, G., Aeronomy, a 20th century emergent science: the role of solar lyman series, *Annales Geophysicae*, *20*, 585–598, 2002.

Kolarski, A., and D. Grubor, Sensing the earth's low ionosphere during solar flares using vlf signals and goes solar x-ray data, *Advances in Space Research*, *53*, 1595–1602, doi:10.1016/j.asr.2014.02.022, 2014.

McRae, W. M., and N. R. Thomson, Vlf phase and amplitude: daytime ionospheric parameters, *Journal of Atmospheric and Solar-Terrestrial Physics*, *62*, 609–618, 2000.

McRae, W. M., and N. R. Thomson, Solar flare induced ionospheric d-region enhancements from vlf phase and amplitude observations, *Journal of Atmospheric and Solar-Terrestrial Physics*, *66*, 77–87, doi:10.1016/j.jastp.2003.09.009, 2004.

Mitra, A. P., *Ionospheric Effects of Solar Flares*, Springer, New York, 1964.

Rakov, A. V., and A. M. Uman, *Lightning Physics and Effects*, Cambridge University Press, 2003.

Said, R. K., Accurate and efficient long-range lightning geo-location using a vlf radio atmospheric waveform bank, Ph.D. thesis, Stanford University, 2009.

Said, R. K., U. S. Inan, and K. L. Cummins, Long-range lightning geolocation using a vlf radio atmospheric waveform bank, *Journal of Geophysical Research*, *115*(D23), doi:10.1029/2010JD013863, 2010.

Sechrist, C. J., Comparisons of techniques for measurements of d-region electron densities, *Radio Science*, *9*(2), 137–149, 1974.

Singh, A. K., A. K. Singh, R. Singh, and R. P. Singh, Solar flare induced d-region ionospheric perturbations evaluated from vlf measurements, *Astrophysics and Space Science*, *350*, 1–9, doi:10.1007/s10509-013-1699-4, 2013.

Tao, X., J. Bortnik, and M. Friedrich, Variance of transionospheric vlf wave power absorption, *Journal of Geophysical Research*, *115*(A7), doi:10.1029/2009JA015115, 2010.

Thomson, N. R., Experimental daytime vlf ionospheric parameters, *Journal of Atmospheric and Terrestrial Physics*, *55*(2), 173–184, 1993.

Thomson, N. R., Daytime tropical d region parameters from short path vlf phase and amplitude, *Journal of Geophysical Research*, *115*(A09313), doi: 10.1029/2010JA015355, 2010.

Thomson, N. R., and M. A. Clilverd, Solar flare induced ionospheric d-region enhancements from vlf amplitude observations, *Journal of Atmospheric and Solar-Terrestrial Physics*, *63*, 1729–1737, 2001.

Thomson, N. R., and W. M. McRae, Nighttime ionospheric d region: Equatorial and nonequatorial, *Journal of Geophysical Research*, *114*(A08305), doi: 10.1029/2008JA014001, 2009.

Thomson, N. R., C. R. Rodger, and M. A. Clilverd, Large solar flares and their ionospheric d region enhancements, *Journal of Geophysical Research*, *110*(A06306), doi:10.1029/2005JA011008, 2005.

Thomson, N. R., M. A. Clilverd, and W. M. McRae, Nighttime ionospheric d region parameters from vlf phase and amplitude, *Journal of Geophysical Research*, *112*(A07304), doi:10.1029/2007JA012271, 2007.

Šulić, D. M., and V. A. Srećković, A comparitive study of measured amplitude and phase perturbations of vlf and lf radio signals induced by solar flares, *Serbian Astronomical Journal*, *188*, 45–54, doi:10.2298/SAJ1488045S, 2014.

Wait, J. R., and K. P. Spies, Characteristics of the earth-ionosphere waveguide for vlf radio waves, *Technichal Note 300*, National Bureau of Standards, 1964.